Origin of Non-Uniform Plasticity in a High-Strength Al-Mn-Sc Based Alloy Produced by Laser Powder Bed Fusion

Dina Bayoumy[1,2], Kwangsik Kwak[3], Torben Boll[4], Stefan Dietrich[5], Daniel Schliephake[5], Jie Huang[6], Junlan Yi[6], Kazuki Takashima[3], Xinhua Wu[1,2], Yuman Zhu[1,2,*], Aijun Huang[1,2,*]

[1] Monash Centre for Additive Manufacturing, 15-17 Normanby Rd, Notting Hill, VIC 3168, Australia

[2] Department of Materials Science and Engineering, Monash University, Clayton, VIC 3800, Australia

[3] Department of Materials Science and Engineering, Kumamoto University, 2-39-1 Kurokami, Chuo-ku, Kumamoto 860-8555, Japan

[4] Karlsruhe Nano Micro Facility (KNMF), Karlsruhe Institute of Technology (KIT), Hermann-von-Helmholtz-Platz 1, D-76344, Eggenstein-Leopoldshafen, Germany

[5] Institute for Applied Materials (IAM-WK), Karlsruhe Institute of Technology (KIT), Engelbert-Arnold-Straße 4, 76131 Karlsruhe, Germany

[6] Aeronautical Manufacturing Technology Institute, Shanghai Aircraft Manufacturing Co., Ltd, 201324, China

---

[*] Corresponding authors.
E-mail addresses: yuman.zhu@monash.edu (Y.M. Zhu), aijun.huang@monash.edu (A.J. Huang)

Abstract

The Al-Mn-Sc based alloys specific for additive manufacturing (AM) have been recently developed and can reach ultrahigh strength and adequate elongation. However, these alloys commonly exhibit non-uniform plasticity during tensile deformation, which is a critical issue hindering their wider application. In this work, the origin of this non-uniform plasticity of the alloys produced by laser powder bed fusion (LPBF) has been systematically investigated for the first time. The results show that the loss of uniform plasticity in the alloy originates from microstructural regions containing equiaxed fine-grains (FGs) (~650 nm in size) at the bottom of the melt pools. In micro-tensile tests, the strength of these FG regions can reach a peak of ~630 MPa. After this, an apparent yield drop occurs, followed by rapid strain softening. This FG behavior is associated with intermetallic particles along grain boundaries and a lack of uniform mobile dislocations during deformation. The columnar coarse-grain (CG) regions in the remaining melt pools show uniform plasticity and moderate work hardening. Furthermore, the quantitative calculations indicate that the solid solution strengthening in these two regions is similar. Nevertheless, secondary Al_3Sc precipitates contribute to ~260 MPa strength in the FG, compared to 310 MPa in the CG due to their different number density. In addition, grain boundary strengthening can reach 230 MPa in the FG region; nearly double the CG region value.

Keywords: Aluminium alloy; Laser powder bed fusion; Crystal plasticity; Microstructures, Strengthening.

1. Introduction

Additive manufacturing (AM) has gained wide interest in the past decade since it can produce near net shape, complex engineering parts with improved cost efficiency [1,2]. Furthermore, AM represents a cleaner production technology capable of conforming to environmental sustainability with a higher material utilization ratio than conventional manufacturing techniques [2]. Laser powder bed fusion (LPBF) is one of the typical AM techniques that has been extensively developed in recent years for many metal and alloy systems [3], including aluminum (Al) alloys. This is mainly due to the growing demand for lightweight structural metals for the transportation and aerospace industries [4]. Initial trials of LPBF in the production of Al alloys have been mainly limited to the near eutectic Al-Si based alloys [5]. However, these Al alloys produced by LPBF, though they have good weldability, usually exhibit limited and anisotropic mechanical performance [2,5,6]. Therefore, the development of high-performance Al alloys specific for LPBF production has been one of the main efforts in recent years [5,7].

One of the significant areas of progress in this aspect has been recently developed scandium (Sc)-containing Al alloys [7–11]. These alloys fabricated by LPBF exhibit superior strength and good ductility [7,11]. Typically, a Sc-modified 5xxx series Al alloy, known as Scalmalloy, can achieve tensile yield stresses exceeding 480 MPa and fracture strain over 8.6% after LPBF and post heat treatment [12]. Moreover, a Sc-reinforced 3xxx series Al alloy (i.e., Al-Mn) was reported to have even higher strength [13–14]. When produced by LPBF, the relative material density exceeds 99.8%. In addition, the alloy can achieve a tensile yield strength of ~430 MPa with a fracture strain of over 17% [13]. After the post heat treatments, the yield strength can reach 550 MPa and the fracture strain exceeds 13% [14]. The excellent mechanical properties of these alloys have been attributed to the addition of adequate Sc, which plays essential roles during LPBF fabrication and post heat treatments, including enhancing LPBF processability, promoting grain refinement, and inducing precipitation-hardening [15]. The common microstructural features of these Sc-containing Al alloys fabricated by LPBF are a bimodal grain structure and a high fraction of intermetallic particles [14,16,17]. During LPBF processing, a high number density of primary Al_3Sc particles has been observed in the melt prior to the solidification of Al. They can then act as inoculants for the formation of refined α-Al grains. Nevertheless, the distribution of these primary Al_3Sc in the melt pool was found to be non-uniform due to the distinct temperature regimes throughout the melt pool [16]. At cooler zones towards the melt pool boundary, the primary Al_3Sc particles can significantly refine the microstructure. Whereas, at hotter regions (> 800 °C) towards the core of the melt pool, they dissolve and thus relatively coarse columnar grain regions form. This leads to the characteristic bimodal grain structures. This bimodal grain distribution has been suggested to be beneficial to the ductility of the alloy [18,19]. Also, primary Al_3Sc has been observed along grain boundaries [11,13,16] and they were suggested to pin grain boundaries effectively and resist their growth during LPBF processing [15,16,20]. Moreover, the ultrafast cooling rates of $\sim 10^6$ K/s in LPBF can retain a certain amount of Sc in the solid solution [16]. On this basis, secondary precipitation can occur by an appropriate post heat treatment, leading to significant precipitation hardening [15] that can further improve the alloy strength.

While the Sc-reinforced Al alloys processed by LPBF can have an excellent combination of ultrahigh strength and good ductility, these alloys usually exhibit a non-uniform plasticity [7,12–14,21–25]. During tensile deformation, a distinct yield point phenomenon, i.e., strain softening, has been observed in the stress-strain curve where the flow stress reaches a yield point followed by a subsequent drop. After the yield drop, the plastic deformation usually continues without apparent work hardening, especially when the Sc content exceeds 0.6 wt.% (eutectic composition in binary Al-Sc alloy) [15]. Similar features have also be observed in the stress-strain curves of conventional hypereutectic Al-Mg-Sc alloys where a superior yield strength (beyond 400 MPa) was attained, then the flow stress exhibited a load drop followed by an extension with limited work hardening [26–28].

Such yield point phenomenon may result in plastic instability, which is a major drawback in the application of these materials. According to the Considère criterion for necking, plastic instability occurs when the increase in strain is not accompanied by an increase in stress [29]. Consequently, a reliable deformation behavior does not merely rely on yield strength but also would incorporate work hardening. In other words, metallic materials without work hardening capacity are potentially unstable since necking is expected to start shortly after the onset of plastic deformation. Till now, however, the origin of the non-uniform plastic deformation associated with these Sc-containing Al alloys remains unclear due to the complex and inhomogeneous microstructure, which hinders any further scheme to improve the mechanical properties of the alloy for real applications. On this basis, the aim of this work is to systematically study the tensile deformation behavior of the Sc-reinforced Al-Mn based alloys produced by LPBF in order to elucidate the microstructural origin of the non-uniform plastic deformation. The results of this work are expected to provide an important basis for any further strategy to deliver this class of additive manufactured Al alloys with excellent mechanical performance.

List of acronyms:

AM	Additive manufacturing
LPBF	Laser powder bed fusion
FG	Fine grains
CG	Coarse grains
LD	Loading direction
TD	Transverse direction
SS	Stress-strain
AF	As-fabricated
HT	Heat-treated
$\sigma_{0.2}$	The stress at a plastic strain of 0.2%
σ_{UY}	Upper yield strength
σ_{LY}	Lower yield strength
OS	Overall strain
LS	Localized strain
LCG	The micro-sample gauge is parallel to the long axis of the coarse grains
SCG	The micro-sample gauge is parallel to the short axis of the coarse grains
BD	LPBF build direction
ND	Direction normal to BD

2. Methods

2.1. Specimen preparation

The alloy powder used in this study was gas atomized out of the designed alloy composition using a vacuum induction gas atomization (VIGA) process. The chemical composition analyzed by inductively coupled plasma atomic emission spectroscopy (ICP-OES) was Al-2.32Mn-1.42Mg-0.56Sc-0.13Zr-0.03Fe-0.04Si (at.%), i.e., Al-4.58Mn-1.24Mg-0.91Sc-0.42Zr-0.07Fe-0.04Si (wt.%). The particle size of the powder was in the range of 20–70 µm with an average value of around 35 µm. The LPBF processing was carried out using a commercial EOS M290 powder-bed machine equipped with a Yb-fiber laser with a wavelength of 1060-1100 nm, maximum power of 400 W, and spot size of around 100 µm. All samples were processed using the LPBF optimized parameters of 350 W (laser power), 1600 mm/s (scan speed), 0.1 mm (hatch distance), and 30 µm (layer thickness) with a laser beam rotation of 67° alternating between consecutive layers. The processing was performed under a controlled Argon environment with a minimum oxygen level of 0.1 vol. %. The post heat treatment was performed in a muffle furnace in air at 300 °C for 6 hours.

2.2. Mechanical testing

2.2.1. Macro-tensile testing and digital image correlation

Flat dog-bone specimens with a gauge length of 10 mm, a width of 5 mm, and a thickness of 5 mm were machined for tensile mechanical testing. Three horizontal samples (with the tensile axis normal to the build direction) were tested for each condition to get an average result. A room-temperature tensile test was performed using Instron 5982 machine at a strain rate of 0.015 min^{-1}. A similar specimen was also used for optical space-resolved 3-dimensional strain monitoring by digital image correlation (DIC) with GOM Aramis professional 2020 software. The specimen gauge was sprayed white and then spotted with black paint to achieve a stochastic pattern in order to get optically traceable reference points.

2.2.2. Micro-tensile testing

Micro-tensile samples with gauge length (L) of 25 µm, width (W) of 10 µm, and thickness (t) of 10 µm were prepared using focused ion beam (FIB) in a NB-5000

HITACHI FIB-SEM microscope, with the gauge section of the sample milled towards the center of a ~3 mm diameter Al disk, as illustrated in Fig. 1(a-c). A piezoelectric actuator with a position accuracy of 10 nm was used for displacement control. The test was performed at a displacement rate of 0.1 µm/s, at room temperature in atmospheric air. The gauge section of the sample for micro-tensile testing was monitored during the test using an optical microscope. The strain measurement was performed via DIC during tensile testing. The load was measured using a load cell with a 200 mN capacity. More details of such a micro-tensile test can be found elsewhere [30].

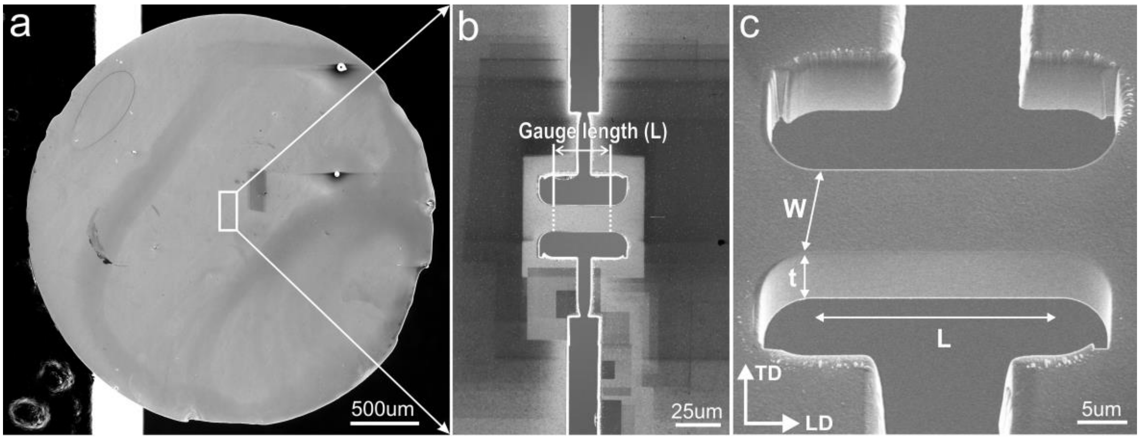

Fig. 1 Sample preparation for micro-tensile testing. (a) Disk with 3 mm in diameter and a thickness of ~10 µm, (b) enlarged FIB image showing the micro-tensile sample taken from the center area of the disk marked by the rectangular frame in (a), (c) high-magnification FIB image showing the gauge length (L), width (W), and thickness (t), LD and TD represent the loading direction and the transverse direction of the micro-tensile sample respectively.

2.3. Microstructure characterization

2.3.1. FIB tomography

The FIB tomography (using the slice-and-view technique) for the intermetallic particles was performed in a FEI Quanta 3D FEG SEM microscope. The overall evaluated volume covered 289 µm^3. A total 452 slices were imaged, with each slice setting to a thickness of 10 nm. Therefore, a total thickness of 4.52 µm was investigated. The image data was binarized in a next step using local binarization (local window radius 45 pixel) with the Phansalkar algorithm [31] (parameters $k = 0.1$, $r = 0.3$, $p = 2$ and $q = 10$). After a morphological opening step to separate image noise from precipitations and to remove the single foreground voxels stemming from image noise, a classic watershed segmentation using the MorphoLibJ [32] Plugin in Fiji [33] was carried out. Following the image manipulation, VGStudio MAX 3.4 (Volume Graphics GmbH, 2019) was used to reconstruct the 3D image from these image slices. The algorithm for defect and inclusion analysis was used to analyze the different labels in the watershed and particle images. Particle size distributions were extracted from the binary image. The labeled particles were filtered using a minimum volume of 8 voxels as a cut-off to avoid the false interpretation of image noise.

2.3.2 Electron microscopy

All the samples for scanning electron microscopy (SEM) imaging were cut along the building direction, then mounted in epoxy resin, ground to 2400 Grit size, and polished using silica colloidal suspension. The backscattered electron (BSE) and electron backscattered diffraction (EBSD) images were acquired in the JEOL 7001F equipped with Oxford Nordlys Max2 EBSD detector. The EBSD data was obtained at an accelerating voltage of 20 kV and a step size of 0.155 µm. The grain size in the coarse-grain region was determined as the mean of the equivalent diameters of the grains based on the EBSD maps. The grain boundary was defined as the misorientation between two points greater than 5°.

For scanning transmission electron microscopy (STEM) imaging, bulk samples were sliced into 0.3 mm thick pieces using a slow-speed saw. These slices were punched into 3 mm diameter discs, ground to ~40 μm in thickness, and then ion-milled in a Gatan Precision Ion Polishing System (PIPS II). The STEM images were obtained using a FEI Titan 80-300 transmission electron microscope operating at 300 kV. The convergence semi-angle was set to 15.0 mrad, leading to a probe diameter of ~0.12 nm. The bright-field (BF-) STEM images were collected in the (semi-) angle range of 0-10 mrad. In high-angle annular dark-field (HAADF-) STEM imaging mode, the camera length was set to give an inner collection semi-angle of ~64 mrad.

2.3.3 Atom probe tomography (APT)

The tip samples for APT were prepared by a Zeiss Auriga Dual Beam FIB using Ga^+ ions. The region of interest was protected by a layer of Pt before milling to avoid the damage caused by the Ga^+ ion beam, as described by Larson et al. [34]. Atom probe acquisition was conducted in a Local Electrode Atom Probe (LEAP) Cameca 4000 XR under ultrahigh vacuum at a base temperature of 50 K. The standing high voltage was controlled by the detection rate set to 0.5%. The device was operated using laser pulsing with a pulse energy of 30 pJ and a pulse repetition rate of 100-200 kHz. The APT data were reconstructed and analyzed using Cameca IVAS 3.6.14 software. The composition of phases was determined using the proximity histogram method [35].

3. Results

3.1. Macro-tensile properties

The typical engineering stress-strain (SS) curves of the alloy in the as-fabricated (AF) and heat-treated (HT) conditions are presented in Fig. 2. For the AF condition, the yield strength, defined as the stress at a plastic strain of 0.2% ($\sigma_{0.2}$), is 395 ± 4 MPa, while fracture strain reaches 22 ± 1 %. The post heat treatment at 300 °C for 6 h further raises the $\sigma_{0.2}$ to 559 ± 4 MPa, which is around 42% greater than that of the AF condition. However, the fracture strain drops to 10 ± 2 %, which is approximately 55% less than that of the AF condition. From both the AF and HT SS curves, the alloy exhibits discontinuous yield during tensile deformation. Specifically, a slight yield drop followed by limited work hardening is observed in the AF tensile curve. Nevertheless, the yield drop becomes prominent in the HT tensile SS curve, where an upper yield strength (σ_{UY}) of 572 MPa is attained, followed by a subsequent yield drop to a lower yield strength (σ_{LY}) of 556 MPa. After the yield drop, a very slight rise in stress can be observed, followed by a plateau of almost constant stress until failure.

The DIC technique was then applied to monitor the local strain distribution during the tensile deformation of the heat-treated sample. The images in Fig. 3(c-g) correspond to the five overall strain levels marked by the dashed lines in the engineering SS curve in Fig. 3(a), i.e., 1%, 2%, 5%, 7%, and 9.8%. The color map reflects the axial strain percentage defined based on the resolution of the optically traceable reference points on the specimen gauge. Two measurements were set by the software. The "overall strain" measures an average strain in between the long black line, similar to a virtual extensometer. In contrast, the "localized strain" measures an average strain in between the small black line, as illustrated in Fig. 3(b). From Fig. 3(c), the overall strain in the gauge is similar to the localized strain at a strain level of 1% (before the yield drop). However, after the yield drop, the axial strain starts to localize on the gauge. Fig. (h-i) shows the evolution of the stress and the corresponding overall strain and localised strain with time. It can be seen that as the overall strain increases from 2 % to 9.8%, the localized strain increases by ~60% relative to the overall strain.

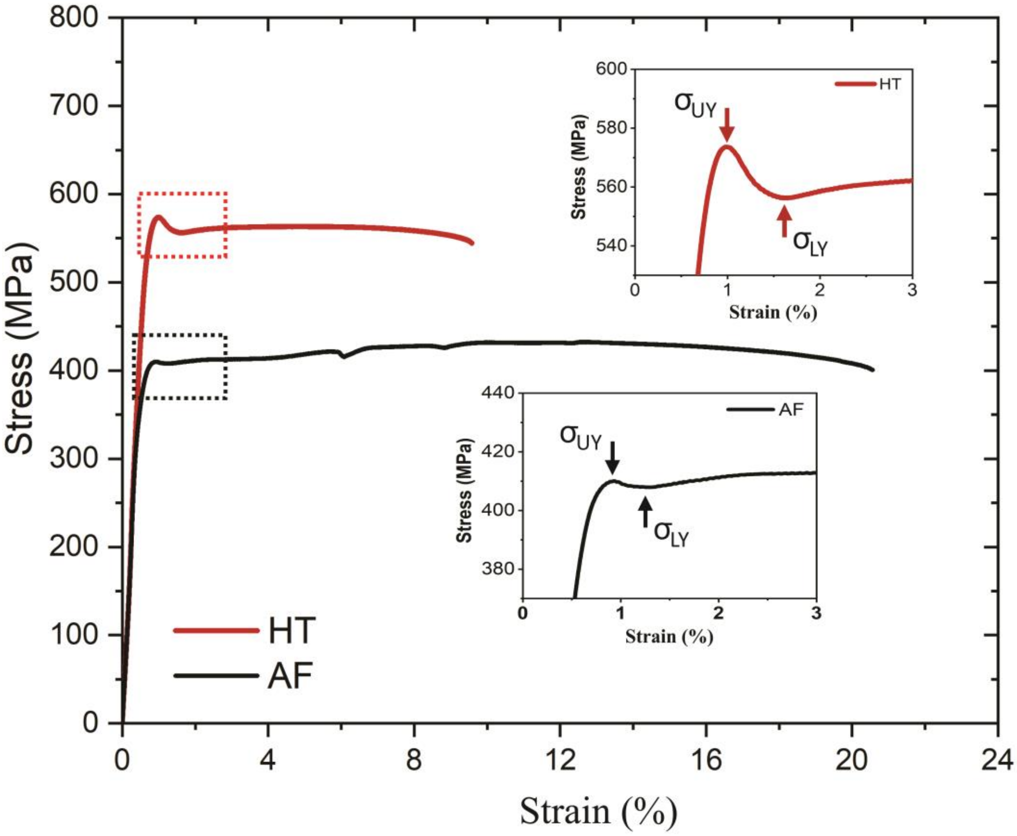

Fig. 2. Engineering stress-strain (SS) curves of the alloy in as-fabricated (AF) and heat-treated (HT) conditions (300 °C/6h). Their local yield regions, as marked by dashed-line frames, are enlarged and inserted for clarity.

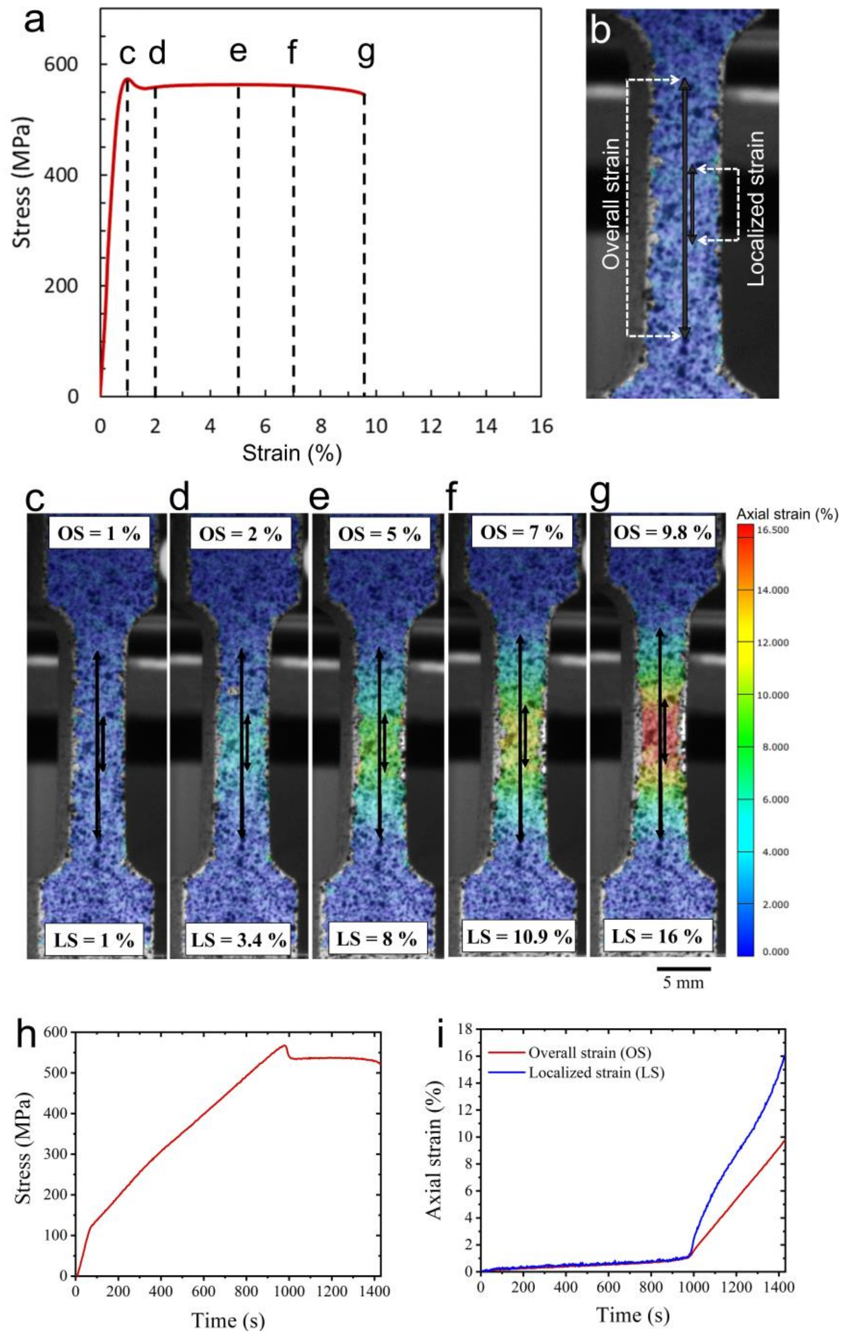

Fig. 3. Strain monitoring by DIC method of a HT specimen during tensile deformation. (a) Five overall strain levels (marked by dashed-lines) selected for DIC images, (b) illustration in the specimen gauge showing the virtual extensometer set for measuring the overall strain (OS) and localized strain (LS), (c-g) DIC maps showing strain fields

forming within the gauge at different strain levels, (h) the evolution of stress with time, (i) the corresponding evolution of OS and LS with time.

3.2 Micro-tensile behavior

To reveal the origin of the apparent yield drop and discontinuous deformation associated with the HT sample shown in Figs. 2 and 3, a micro-tensile test was performed. This is based on the characteristic bimodal grain structure of this alloy. As shown in Fig. 4(a), the microstructure of the HT sample is made of alternating layers of fine-grain (FG) and coarse-grain (CG) regions. This bimodal grain structure has also been observed in the AF condition [13]. The CG is elongated, and its long axis is nearly parallel to the build direction. This region shows a relatively strong orientation texture, as can be seen in Fig. 4(b). Most grains in the CG region have a width range between 2 μm and 6 μm, as shown in Fig. 4(d), with the aspect ratio between 1.5 to 10. In contrast, the grains in the FG region are equiaxed with a size range from 0.1 to 1 μm and a mean diameter of 0.65 ± 0.20 μm, as shown in Fig. 4(e). There is a less preferable orientation in this FG region, supported by the relatively week texture from the corresponding pole figure in Fig. 4(c). According to the characteristic bimodal grain structures, the micro-tensile samples were taken separately from the CG and FG regions. In the CG region, the samples were made from two grain directions, one with the gauge parallel to the long-axis of coarse grains (LCG) while the other parallel to the short-axis of coarse grains (SCG), as illustrated in Fig. 4(a). There is no special direction for preparing the micro-tensile sample from the FG region.

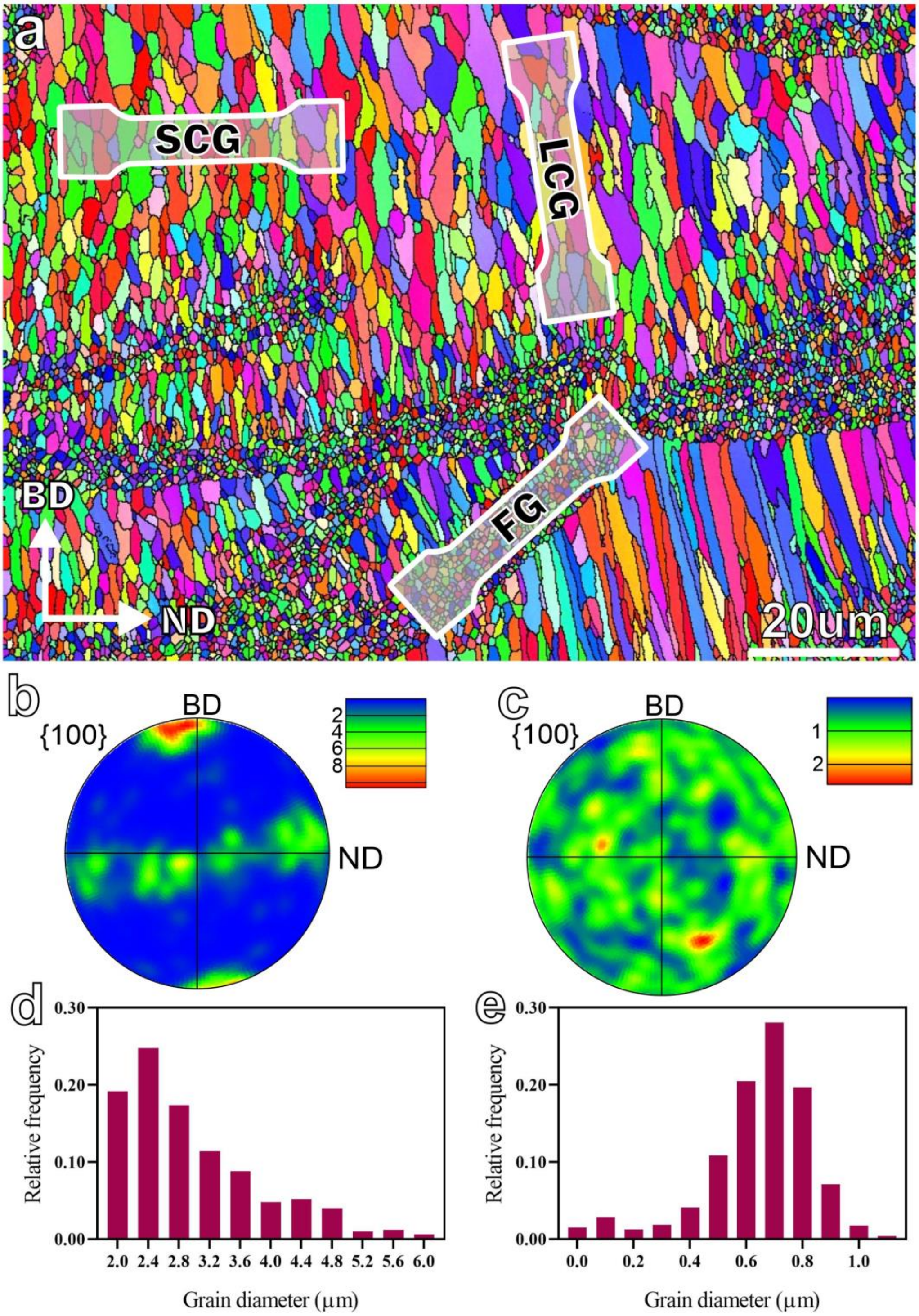

Fig. 4. Typical bimodal grain structure in the HT sample. (a) EBSD inverse pole figure (IPF) map showing alternating FG and CG regions. The samples for micro-tensile testing are also shown, the IPF map is generated by choosing build direction (BD) as the projection axis, ND is the direction normal to BD. (b-c) Corresponding pole figures from

CG and FG regions, respectively. (d-e) Grain size distribution of CG and FG regions respectively.

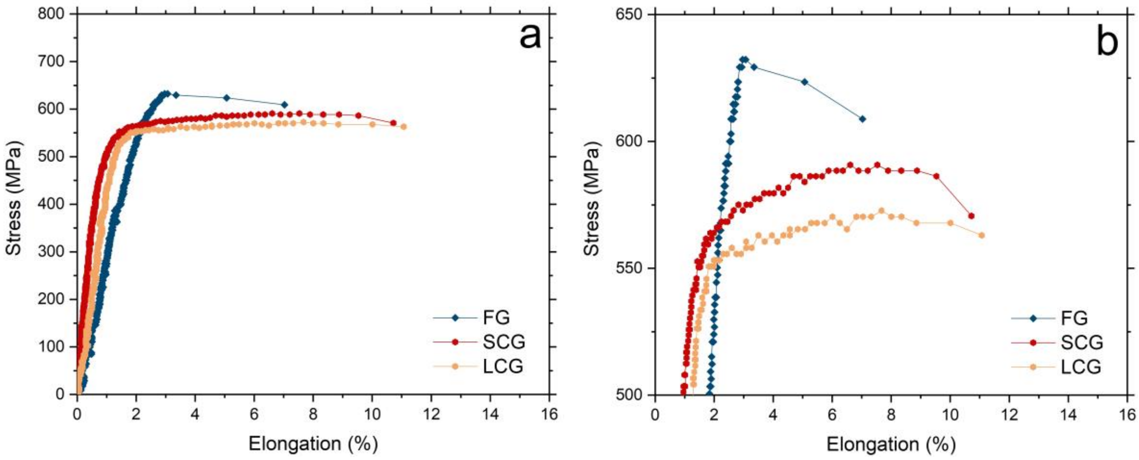

Fig. 5. Stress-strain curves from the micro-tensile testing. (a) Engineering stress-strain curves of the FG, SCG, LCG micro-tensile specimens, (b) close-up view at the tensile stress level beyond 500 MPa.

Fig. 5(a) provides the SS curves of micro-tensile samples taken along SCG, LCG, and from FG regions. Inspection of these tensile curves reveals different deformation behavior between the FG and CG regions. At first glance, the yield drop can be seen in the FG curve while it is absent in two CG curves. Close inspection of FG's SS curve, Fig. 5(b), shows an abrupt transition from the elastic to the plastic deformation until an upper yield point σ_{UY} (632 MPa). After reaching σ_{UY}, the plastic stress continuously decreases as the strain increases. Unlike FG, both the LCG and SCG curves exhibit a smooth transition from elastic to plastic deformation without yield peak and drop. The stress gradually rises as the strain increases, showing a discernible work-hardening effect. Specifically, SCG shows a lower yield strength ($\sigma_{0.2}$) of 493 MPa than LCG (526 MPa), Table 1. However, the UTS of SCG reaches 591 MPa, which is higher than LCG (573 MPa), suggesting a slightly stronger work hardening effect of SCG compared to LCG. In addition, a uniform elongation of ~7.5% can be seen in both the LCG and SCG SS curves. Given that both the SCG and LCG SS curves exhibit such uniform plasticity, it seems even clear that the overall non-uniform plasticity of the alloy shown in Fig. 2 is mainly due to the regions constituting FGs.

Table 1 Mechanical property values from micro-tensile and macro-tensile curves of the alloy in HT condition.

	$\sigma_{0.2}$ (MPa)	σ_{UTS} / σ_{UY} (MPa)
LCG	526	573
SCG	493	591
FG	576	632
Macro-property values	559 ± 4	572 ± 9

3.3 Microstructure

The distinct tensile behavior of FG and CG has been evidenced from the micro-tensile testing for the alloy after heat treatment. To fully understand such a difference, we systematically examine the microstructure in these two regions. As shown by the SEM-BSE images in Fig. 6(a-b), there is a high number density of intermetallic particles existing in both the FG and CG regions and they show a brighter contrast than the matrix. Through FIB tomography and slice and view analyses, Fig. 6(c-d), the volume fractions of these intermetallic particles were obtained. The results reveal that the intermetallic particles in the FG region have a volume fraction of ~6.8%, which is much higher than the CG region (4.2%).

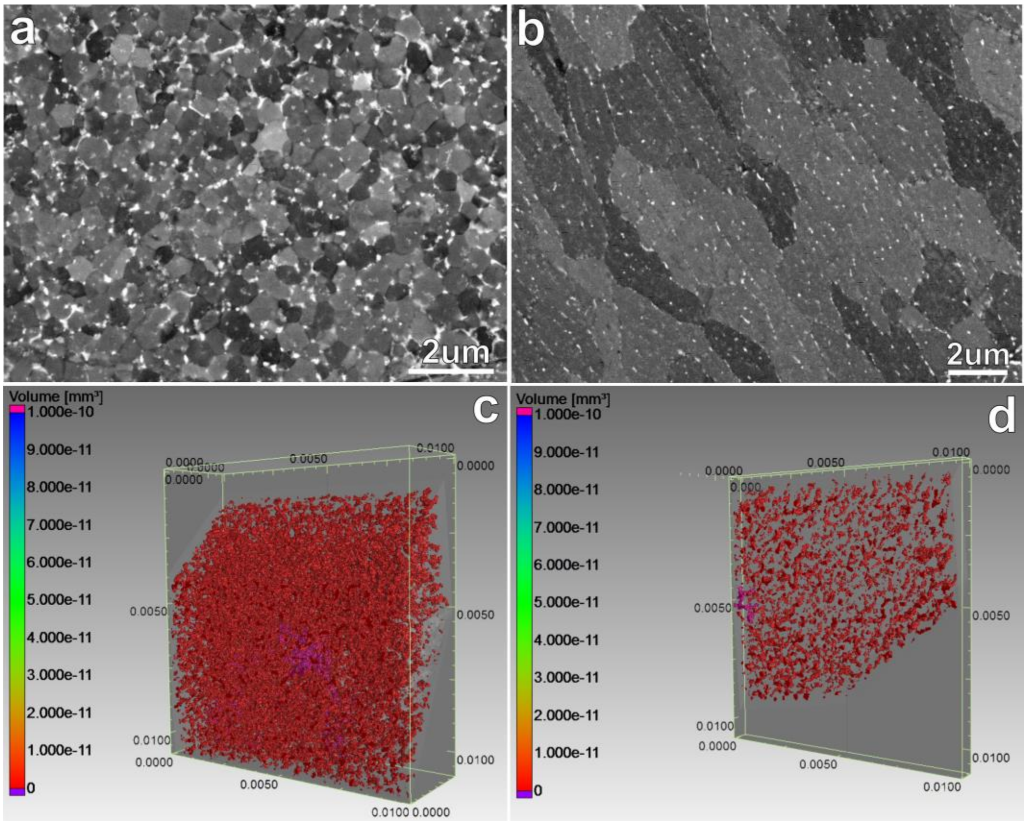

Fig. 6. Intermetallic particles in FG and CG regions. SEM-BSE image taken from (a) FG and (b) CG regions of a HT sample, showing a high number density of intermetallic particles forming in both areas. (c-d) 3D visualization reconstructed from the FIB slice-and-view images showing the intermetallic particles in the FG region and CG region, respectively.

Apart from these relatively large intermetallic particles, nano-scale precipitates subject to HT have also been suggested in previous work [11,14,36]. Therefore, APT was employed to reveal such small particles. Fig. 7 provides three-dimensional elemental reconstruction maps of an APT sample taken from the FG region. This map also includes a segment of a grain boundary. From these, one can see that the main alloying elements, i.e., Mn and Mg, are nearly uniformly distributed in the matrix. In comparison, most of the Sc exists in clusters with a size range between 2 nm and 3 nm, as shown in Fig. 7(c). Furthermore, there is no noticeable precipitate-free zone near the grain boundary. Similar feature has been also observed in the CG region.

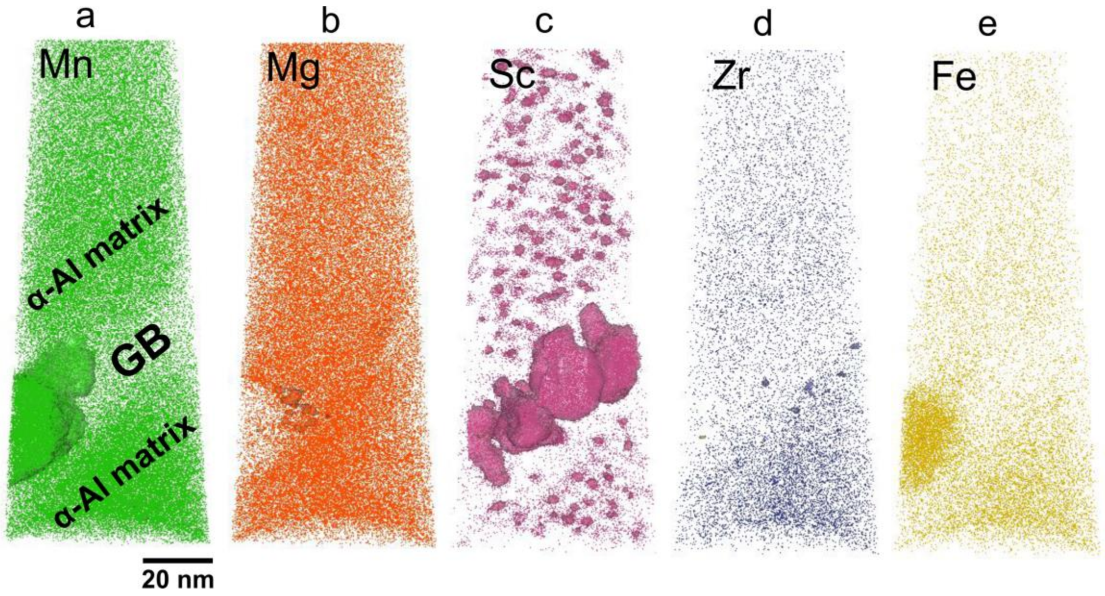

Fig. 7. APT 3D reconstructed composition maps from a FG region of the HT sample.

Those intermetallic particles along the FG boundaries observed in Fig. 6(a) are also evidenced by APT. According to elemental maps shown in Fig. 7, the irregularly-shaped particle in the left part of the grain boundary is mainly made of Al, Mn, and some Fe. Another type of particle distributed in the grain boundary, without overlapping with the Mn/Fe-rich particle, mainly contain Sc element besides Al. These grain boundary particles have been characterized as $L1_2$ Al_3Sc and Mn(Fe)-rich quasicrystal in our recent work [13]. Also, there are a limited number of tiny Zr-rich and Mg-rich particles, mainly existing at the interface between α-Al and grain boundary particles, Fig. 7(b) and (d). A detailed cluster finding analysis based on the APT data was performed to determine the volume fraction of the Sc-rich precipitates observed in FG, as displayed in Fig. 7c. It should be emphasized that similar fine Sc-rich precipitates have been observed in the corresponding CG regions. The results listed in table 2 revealed that the nano-scale precipitates in the CG region have a higher number density (2.41×10^{24} m^{-3}) and volume fraction (1.68%) than those in the FG region (1.85×10^{24} m^{-3} at a volume fraction of 1.16%). Nevertheless, the average radius of the precipitates has similar values of 1.15 ± 0.25 nm and 1.19 ± 0.30 nm in the FG and CG regions, respectively (Table 2). These sizes are very close to that reported in Scalmalloy (~1.1 nm in the heat-treated condition) [36].

Table 2 The cluster analysis results in FG and CG from APT data.

	Volume fraction (f) (%)	Number density (N) (m^{-3})	Average radius (r) (nm)
FG	1.16	1.85×10^{24}	1.15 ± 0.25
CG	1.68	2.41×10^{24}	1.19 ± 0.30

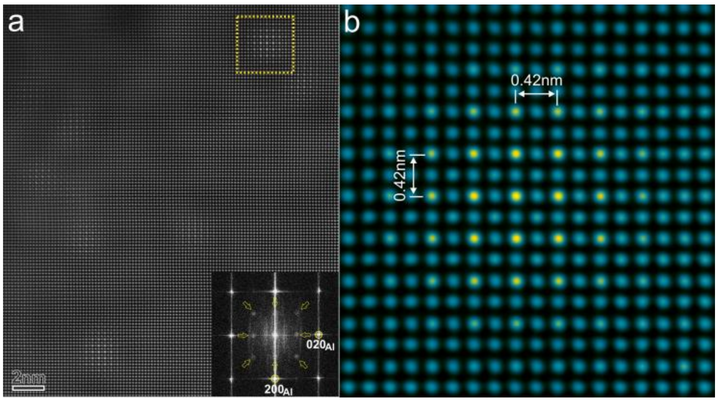

Fig. 8. Secondary precipitates in the matrix of HT sample. (a) HAADF-STEM image taken along $<001>_{\alpha}$ displaying a high number density of nano-sized precipitates finely dispersed in the HT sample. Corresponding FFT pattern inserted showing the diffraction

spots from these precipitates, indicated by holy arrows. (b) Enlarged image showing the $L1_2$ structure (a = 0.42 nm) of the precipitate marked by yellow-color dashed-line frame in (a).

Fig. 8(a) provides a HAADF-STEM image showing the structure of the nano-sized precipitates existing in the α-Al matrix that has been revealed by APT, Fig. 7c. In this $<001>_\alpha$ viewing direction, the bright dots in the image are Sc-rich columns since the intensity of the atomic column in a HAADF image is approximately proportional to the square of the atomic number of the element (the atomic number is 13 for Al and 21 for Sc). From the enlarged image for a single precipitate in Fig. 8(b), the Sc-rich columns are regularly arranged with a separation distance of 0.42 nm in both the horizontal and vertical directions measured from the image. These features confirm that these precipitates have the ordered $L1_2$ structure, which is identical to that of Al_3Sc in previous works [15,37]. However, the core-shell structures corresponding to the Al_3(Sc, Zr) precipitates have not been observed in the APT composition map in Fig. 7d.

Having quantitatively clarified the distinct microstructure features existing in the CG and FG regions after HT, a sample after a tensile strain of 5% was further examined to reveal the deformation behavior of the different microstructures in these two regions. In the FG region, a relatively high number density of tangled dislocations has been observed in some grain interiors, as presented in Fig. 9(a). However, there are still many grains that contain very few dislocations and are clear of dislocation tangles. As a typical image shown in Fig. 9(b), very limited dislocations lines can be spotted either close to the grain boundary or at the particle/matrix interface. On the other hand, the CG region exhibited a more uniform deformation structure. All of the analyzed CG grains have tangled dislocations, which are uniformly distributed in the grain interior, as shown in Fig. 10(c).

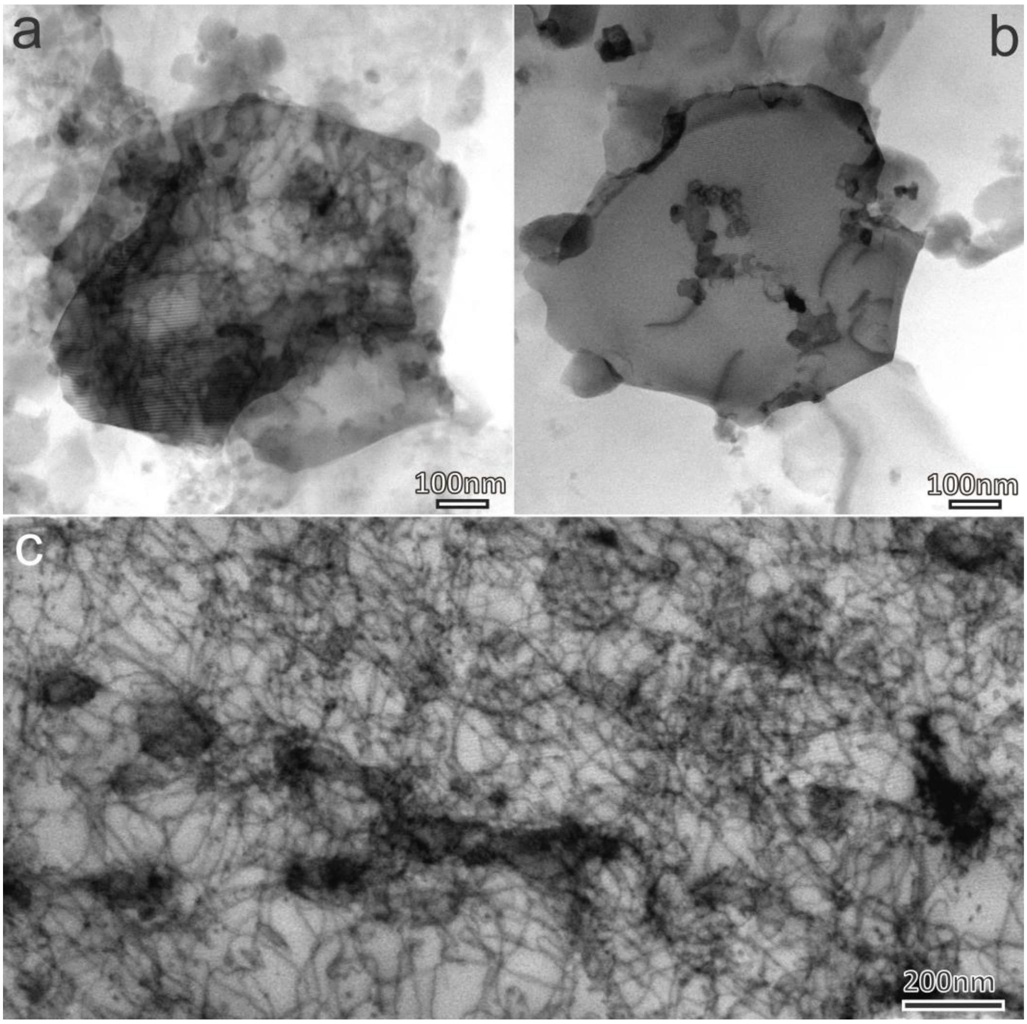

Fig. 9. BF-STEM images of HT sample with 5% tensile strain revealing the dislocation structure inside (a-b) two different grains in FG region, and (c) a grain in CG region. Beam directions in (a-c) are parallel to <110>$_{Al}$**.**

4. Discussion

4.1. Non-uniform plasticity

In this work, an ultrahigh strength (peak strength of 632 MPa) associated with the FG has been revealed by micro-tensile testing. However, such a high strength comes at the expense of work hardening capacity. The FG flow stress reaches the peak at the early stage of the plastic deformation. No further rise of flow stress takes place beyond the σ_{UY}. Instead, macroscopic necking takes place at an early stage of plastic deformation. This can be understood from the Considère condition for plastic instability [38]:

$$\sigma \geq \frac{d\sigma}{d\varepsilon} \tag{1}$$

where σ is the true flow stress, ε is the true strain and $\frac{d\sigma}{d\varepsilon}$ is the work hardening rate. As can be seen from Fig. 5(b), no work hardening occurs in the FG SS curve after the yield drop. In this case, the Considère criterion is satisfied in the low strain range. As a result, plastic instability (i.e., the condition at which necking will propagate in tensile test) is expected to occur at a very early stage of tensile deformation, which in turn limits the uniform elongation of FG. In the CG region, however, both the LCG and SCG tensile curves exhibit a smooth transition from the elastic to the plastic regime without a yield drop; opposite to the strain-softening observed in FG. Furthermore, the SS curve of SCG exhibits a slightly higher level of work hardening than LCG. The reason for this might be that the short axis of the grain (grain width) is aligned perpendicular to the loading axis of the SCG specimen. Consequently, the dislocation pile-ups at the grain boundary can enhance the dislocation retention inside the grains.

The loss of uniform plastic deformation has been observed in various Al alloys with ultrafine grain structures, including pure Al (99.99%) [39], commercial 1100 Al [40], AA1050 [41], AA1050 [42], AA8014 [43], Al-6Ni [44], and AA5754 [45]. The detailed analyses provided by these studies have confirmed that the loss of work hardening capacity will occur once the size of grains reduces to ~ 1 μm and below. In this case, plastic instability (necking) will appear at the early stage of plastic deformation [40–42,46]. Therefore, the uniform elongation (the elongation measured at the maximum stress prior to necking or fracture) in ultrafine-grained materials becomes very limited. The yield point phenomenon has been previously explained by two main mechanisms, i.e., dislocation-locking by solute atoms and the shortage of mobile dislocations. In the dislocation-locking mechanism, the yield point phenomenon occurs due to the interaction between the interstitial [47] or substitutional solute atoms [48] and dislocations. Higher stress is required to unlock the solute-pinned dislocations and make the initial movement, producing an upper yield point. Then, the escaped dislocations result in a subsequent yield drop to a lower yield point. In the dislocation-shortage mechanism, by comparison, the lack of mobile dislocations due to the shortage of dislocation sources in relatively small grains can lead to inhomogeneous flow stress [41,44]. Once the grain size drops below the dislocation slip distance, the dislocation accumulation within the grains will be suppressed during deformation [49]. In this situation, these dislocations tend to aggregate at the grain boundaries. In the current work, the TEM investigation for the strained FG regions, Fig. 9(b), has revealed very limited dislocations in many grains. This lack of dislocations implies that the non-uniform plastic deformation observed in FG tends to be dominated by the dislocation-shortage mechanism. The lack of mobile dislocations to initiate the deformation in many fine grains is the reason for the yield phenomenon [41]. Also, having dislocations trapped at grain boundaries, instead of being uniformly distributed within the grains, as can be seen from Fig. 9b, can promote the annihilation rate of dislocations in FG grains [44,50,51] and enhance the dynamic recovery of dislocations during deformation. As a result, the absent dislocation accumulation ability revealed in FG grains leads to a loss in the work hardening capacity. On the other hand, the yield peak did not appear in CG, and our observations reveal a high number density of mobile dislocations in this region that can comply with the applied strain. As a result, a smooth transition from the elastic to the plastic regime has been observed in CG regions.

In order to maintain the hypereutectic concentration in our alloy, an amount of Sc of 0.91 wt.% has been used. It worth mentioning that this value was kept higher than the eutectic equilibrium Sc concentration (~ 0.6 wt.%) to account for the possible increase in Sc solubility at LPBF high cooling rates, which might shift the eutectic concentration to the right. Consequently, additional primary Al_3Sc particles form during solidification [13]. A higher number density of primary intermetallic particles forms in FG regions compared to CG, as confirmed by the FIB slice and view analysis presented in Fig. 6. One possible reason for this non-uniform density distribution of the particles might be the higher volume fraction of grain boundaries in the FG region that might act as fast diffusion paths for the solute elements, leading to the rapid diffusion and growth of the Mn and Sc-rich intermetallic particles [52]. It seems that the strain-softening phenomenon appearing in the micro tensile curve of FG is closely related to the cavitation of these grain boundary particles. As evidenced by the SEM studies on the fractured specimen, Fig. 10(a), microcracks normally initiate from the hard FG region. Moreover, many micro-voids can be observed at the matrix/particle interface of this FG region, Fig. 10(b). With any progression of plastic strain, these micro-voids are expected to grow and link, forming microcracks that preferably propagate intergranularly along the intermetallic phases in the grain boundaries. A similar fracture was also reported in 7010 Al alloy [53]. In that work, it was suggested that the flow localizes in narrow shear bands as plastic deformation grows ahead of a propagating crack tip. Then, at a certain critical strain, the interface between the matrix and the particles decoheres. With the onset of decohesion, the resistance to flow will dramatically drop, and the unzipping of the particles from the matrix within the shear band will take place, leading to a fast shear fracture process. Therefore, the size and distribution of the particles and the resistance of the matrix/particle interface to decohesion are all determinantal for the fracture process [4]. In this work, there is a high number density of intermetallic particles that are closely spaced along the grain boundaries in the FG region. They are expected to provide an easy path for the crack extension at these intermetallic sites. Though Mn-rich and Sc-rich intermetallic particles play an effective role in pinning grain boundaries [13,16], special care must be taken to control particle size and number density since fractographic features in this study imply that large segregations at the grain boundary can promote fast intergranular fracture. Note that the intragranular secondary precipitates are much finer than the particles forming at the grain boundaries and they are uniformly distributed within the matrix. Hence, they should not contribute directly to the decohesion process [53].

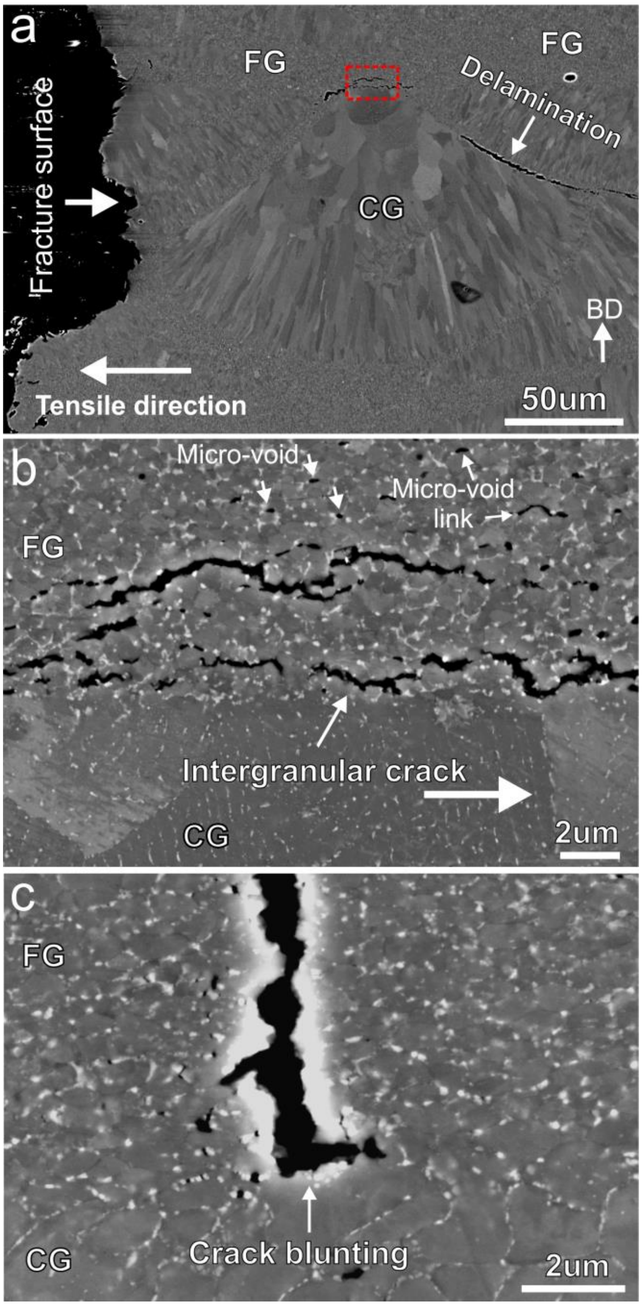

Fig. 10. HT sample strained to fracture. (a) SEM image of tensile fracture surface showing micro cracks occurring in FG and interface delamination, (b) enlarged image from red-color dashed-line rectangle frame in (a) showing the nucleation of microvoids due to grain boundary particles decohesion followed by progressive linkage of microcracks propagating along the grain boundary, (c) SEM image showing a crack blunting at the CG region.

Since the CG plastically deforms prior to the FG, as revealed by micro tensile curves in Fig. 5(a), the FG sustains most applied stress till σ_{UY}. This led to a decrease in the yield strength of the bimodal alloy compared to the FG (Table 1). Furthermore, the difference in flow stress between FG and CG is expected to generate a heterogeneous stress distribution throughout the microstructure. Such inhomogeneity and strain localization has also been observed at the interface between FG and CG regions in bimodal Al-Mg alloy [54,55]. The strain was localized mainly within the CG, which is not surprising since the CG has greater dislocation plasticity compared to FG during deformation. Therefore, micro-cracks are expected to nucleate at interfacial regions when large strain inhomogeneity occurs [55]. This can lead to the delamination that has been observed in the fractured microstructure in this work, Fig. 10(a). Such delamination was suggested to be associated with a crack-retarding mechanism, by which the tensile ductility of the bimodal alloy can be enhanced [56]. When the microcrack encounters the CG colony during its fast propagation, the CG will retard its propagation by blunting the crack tip, as can be seen in Fig. 10(c). Consequently, the improved work hardening and uniform elongation in CG can enhance the overall ductility of the alloy. The failure mechanism observed in this study is in good agreement with those reported for Al alloys with bimodal microstructures [56–58].

Indeed, controlling the grain size in FG might be one effective way to alleviate the non-uniform plastic deformation caused by the formation of FG regions. Increasing the grain size beyond 1 μm can reduce the rate of the dynamic recovery and improve the work hardening capacity [41]. In addition, controlling the volume fraction and distribution of intermetallic particles can improve the fracture resistance of the alloy. The

LPBF processing parameters has been found to be critical in controlling the in-process microstructural features. The size and volume fraction of the ultrafine equiaxed grains are proven to be sensitive to the laser energy density, in addition to the base plate heating [59,60]. In addition, upgrading the alloy design by reducing the solute contents can further reduce the number of intermetallic particles. In order to further improve the structural potential of LPBF, these aspects might be considered for future alloy design of Sc-reinforced Al alloys.

4.2. The operative strengthening mechanisms in FG and CG

The micro-tensile testing in this work has revealed that the FG and CG regions exhibit different yield behaviors. In addition, the characteristic microstructural features in these two grain regions have been quantified. On this basis, their strength mechanism can be evaluated. Three main aspects contributing to the strength are considered here [14], i.e. grain boundary strengthening (Hall-Petch), precipitation hardening, and solid solution strengthening.

One of the potent effects of Sc in Al alloy has been suggested to be grain refinement due to the formation of primary Al-Sc particles in the melt prior to the solidification of α-Al [15]. Additionally, due to the ultra-fast cooling rate (up to 10^6 K/s) associated with LPBF, these primary Al_3Sc tend to distribute at the melt pool boundary, where it has a higher survival rate at the lower thermal gradient areas [16]. This non-uniform precipitation leads to the formation of FG and CG bimodal grain architecture. It is worth noting, though, that the average grain size in CG is still finer than grain sizes reported in Al-Si [61]. Here, the yield strength contribution from the grain boundary strengthening in FG and CG regions is estimated by the standard Hall-Petch relation [62]:

$$\sigma_{GB} = \sigma_o + \frac{k_y}{\sqrt{d}} \tag{2}$$

where d is the average grain diameter, σ_o is the lattice frictional stress, and k_y is the Hall-Petch slope. For the sake of simplicity, a similar value of σ_o (20 MPa) was used for both the FG and CG regions [63]. A k_y value of 0.17 MPa $m^{1/2}$ was selected as a reasonable value for FG and CG. This k_y was determined experimentally for an Al-2Mg-2Li alloy [64] and represented the grain boundary strengthening in a similar alloy system [26]. The grain diameter of FG has been measured to be 0.65 ± 0.2 µm in FG and 3.06 ± 1.04 µm in CG. According to Eq. (2), therefore, the grain boundary strengthening contribution to the yield strength of the alloy can be calculated to be 231 MPa in FG and 117 MPa in CG. Therefore, the grain boundary strengthening in FG is nearly double that in the CG region.

Considerable secondary nano-sized precipitates have been observed in both the FG and CG regions subject to the post heat treatment. Their number densities in both regions exceed the value reported in the Scalmalloy (5×10^{23} m^{-3}) with a significant margin. This is mainly due to the higher Sc content in the current alloy (0.91 wt.%) compared to Scalmalloy (0.66 wt.%) [36]. However, a lower number density of these nano-sized particles forms in FG than in CG regions, as revealed by Table 2. This result suggests that the precipitation of secondary particles has been affected by the higher number density of primary Sc-rich particles in FG regions. They scavenge more Sc atoms from the matrix, leading to the lower number density of secondary Al_3Sc precipitates in FG. Previous studies [26,65,66] have indicated that precipitation strengthening is affected by the type of precipitates in terms of their size, shape, and distribution in the matrix. The shearing mechanism (i.e., dislocations shear the precipitate) is more energetically favorable for coherent precipitates with a small radius (< 8 nm) [37,67]. On the other hand, the Orowan dislocation looping mechanism (i.e, dislocations bypass the precipitate) is the common operative mechanism for the relatively large precipitates (> 8 nm) [67]. Given the size of secondary Al_3Sc coherent precipitates smaller than 3 nm in this study, the shearing mechanism is adopted here to estimate their contribution to the strength in FG and CG regions, and it is calculated by [37,66–69]

$$\sigma_{ps} = \sigma_{ms} + \sigma_{cs} \tag{3}$$

where σ_{ms} is the modulus mismatch strengthening, and σ_{cs} is the coherency strengthening. The σ_{ms}, arising from the mismatch between the shear modulus of the Al matrix and the precipitates, can be estimated using the equation [37,66–69]

$$\sigma_{ms} = 0.0055M(\Delta G)^{\frac{3}{2}}\left(\frac{2f}{G}\right)^{\frac{1}{2}}\left(\frac{r}{b}\right)^{\left(\frac{3m}{2}-1\right)} \tag{4}$$

where M is the mean matrix orientation factor (3.06 for Al), ΔG is the difference in the shear modulus between Al and precipitates (42.6 GPa), G is the shear modulus of Al (25.4 GPa), b is the magnitude of Burgers vector (0.286 nm), m is a constant (0.85) [66], r is the mean radius of precipitates and f is their volume fraction. According to Eq. (4), the value σ_{ms} is calculated to be 207 MPa for FG and 252 MPa for CG.

The σ_{cs}, the strain-field interaction between the precipitates and dislocations, is estimated using the equation [37,66,68,69]

$$\sigma_{cs} = M\chi(G\varepsilon)^{\frac{3}{2}}\left(\frac{rf}{0.5Gb}\right)^{\frac{1}{2}} \tag{5}$$

where χ is a constant of 2.6 for face-centered cubic (fcc) metals [66,69], ε is a mismatch parameter estimated by $\varepsilon = \frac{2}{3}\delta$, and δ is the lattice parameter mismatch between precipitates and the Al matrix at room temperature [67]. Therefore, the σ_{cs} contribution to the strength is calculated to be 51 MPa for FG and 62 MPa for CG. It worth pointing out that the primary intermetallic particles might contribute little strengthening by the

Orowan mechanism. However, their contribution was neglected due to the large size of these particles compared to the secondary coherent Al_3Sc precipitates, which are more uniformly distributed in the microstructure. Then the total contribution of the secondary precipitates to the strength according to Eq. (3) is determined to be 258 MPa (207 MPa + 51 MPa) in FG and 314 MPa (252 MPa + 62 MPa) in CG. From the calculated results, the precipitation strengthening in CG is stronger than that from the FG.

Based on the APT results in this work, there are still alloying elements in the matrix in the solid solution state. Typically, the Mn in solid solution is around 1.9 at. % in both the FG and CG regions. In other words, around 18% of the initial content of Mn exists in the intermetallic phases in Fig. 6(c-d). As for Mg, the atomic concentration is around 1.3 at.% in FG and 1.1 at.% in CG, which is lower than the nominal composition (1.42 at. %) of the alloy. Such a difference is mainly attributed to the localized heating source in LPBF that can lead to the partial evaporation of Mg during LPBF processing, given its volatile nature [2,36]. The yield strength increase due to the solid solution can be estimated using the equation [70]

$$\sigma_{SS} = \mathrm{H}C^n \tag{6}$$

where C is the concentration of the solute in atomic percentage, H is a strengthening coefficient, and n is a concentration exponent. Both H and n depend on the solute species, and they have been estimated in reference [63]. Based on Eq. (6), the solid solution strengthening of Mn and Mg is 118 MPa in FG and 116 MPa in CG. The amount of Sc remaining in solid solution (< 0.1 at.%) presumably has a negligible contribution to the solid solution strengthening effect.

The calculation results of strengthening contribution from grain boundaries, secondary precipitates, and solid-solution alloying elements are summarized in Table 4.

Based on these values, the total calculated yield strength ($\sigma_{0.2}$) is 607 MPa in the FG region and 547 MPa in the CG region. The values generally agree well with the experimental tensile strength acquired by the micro-tensile testing. For FG, the calculated yield strength exceeds the experimental value by 31 MPa. Similarly, the calculated strength of CG is 37 MPa higher than the experimental micro-tensile value (average value of ~510 MPa from SCG and LCG). This difference is likely due to the sensitivity of the micro-tensile test. The small gauge thickness from the FIB milling, together with the specific site testing, might give rise to the yield strength discrepancy.

Table 3 Calculated strength contribution from different strengthening mechanisms.

Strengthening contribution	FG (MPa)	CG (MPa)
Grain boundary (σ_{GB})	231	117
Secondary particle ($\sigma_{ms} + \sigma_{cs}$)	258	314
Solid solution (σ_{ss})	118	116
Total strength	607	547

5. Conclusions

In this study, we systematically investigated the tensile behavior of the high-strength Al-Mn-Sc based alloy that has been specifically developed for AM. Micro-tensile testing has been employed to reveal the different plasticity behaviors associated with two microstructural areas forming in the alloy with different grain sizes and morphologies. The related microstructural features, including intermetallic particles and precipitates, have been characterized and quantified in the heat treatment condition to explain different tensile behavior in these two grain areas. The main findings can be summarized as follows:

(1) The alloy exhibits non-uniform plasticity during tensile deformation, which mainly originates from those microstructural areas containing fine grains with an average size range of ~650 nm. Such a grain area existing in the alloy, especially after the post heat treatment, leads to the obvious yield point phenomenon occurring at an ultrahigh upper yield strength of 632 MPa followed by continuous strain softening.

(2) The absence of work hardening in the FG area is attributed to the lack of mobile dislocations and a high density of intermetallic particles along grain boundaries. In comparison, the CG region exhibits a moderate work hardening in two tested directions due to the high number density of tangled dislocations inside the grains during deformation.

(3) The strain-softening phenomenon appearing in the FG micro-tensile curve is closely related to the decohesion of the intermetallic particles aggregating at the grain boundary, which leads to the fast propagating intergranular fracture. The CG regions mitigate the propagation of intergranular cracks originating from the FG area by crack blunting and delamination at their interfaces during plastic deformation, which maintains the overall ductility of the alloy.

(4) Apart from the similar solid-solution strengthening effect, the grain boundary and precipitation strengthening in two grain areas are different. In the FG region, the grain boundaries contribute a higher strength increment of ~231 MPa compared to ~117 MPa in CG region. Nevertheless, the precipitates formed during heat treatment lead

to a larger strength contribution of ~314 MPa in CG grains, compared to ~258 MPa in the FG area, because of their higher number density in the CG region.

Acknowledgement

This work was financially supported by "Industrial Transformation Research Hub for Transforming Australia's Manufacturing Industry through High Value Additive Manufacturing" of the Australian Research Council (grant No. IH130100008). The authors wish to acknowledge the use of instruments and scientific and technical assistance at the Monash Centre for Electron Microscopy (MCEM) as a Node of Microscopy Australia (grant No. LE0454166) and the Karlsruhe Nano Micro Facility (KNMF) in Germany (proposal No. 2020-023-028430). The authors thank Mr. Nick McDougall for the help in performing the FIB slice-and-view experiment and Delphine Chassaing for the FIB preparation of APT tips.

References

[1] L. Bian, N. Shamsaei, J.M. Usher, Laser-Based Additive Manufacturing of Metal Parts: Modeling, Optimization, and Control of Mechanical Properties, first ed., CRC press, London, NewYork, 2017.

[2] N.T. Aboulkhair, M. Simonelli, L. Parry, I. Ashcroft, C. Tuck, R. Hague, 3D printing of Aluminium alloys: Additive Manufacturing of Aluminium alloys using selective laser melting, Prog. Mater. Sci. 106 (2019) 100578.

[3] T. DebRoy, H.L. Wei, J.S. Zuback, T. Mukherjee, J.W. Elmer, J.O. Milewski, A.M. Beese, A. Wilson-Heid, A. De, W. Zhang, Additive manufacturing of metallic components – Process, structure and properties, Prog. Mater. Sci. 92 (2018) 112–224.

[4] I. Polmear, D. St. John, J.F. Nie, M. Qian, Light Alloys: Metallurgy of the Light Metals, fifth ed., Elsevier, Oxford, 2017.

[5] S. Lathabai, Additive Manufacturing of Aluminium-Based Alloys and Composites, in: R.N. Lumley (Ed.), Fundamentals of Aluminium Metallurgy: Recent Advances, Elsevier, 2018, pp. 47–92.

[6] P. Rometsch, Q. Jia, K. V. Yang, X. Wu, Aluminum alloys for selective laser melting – towards improved performance, in: F. Froes, R. Boyer (Eds.), Additive Manufacturing for the Aerospace Industry, Elsevier, 2019, pp. 301–325.

[7] Q. Jia, P. Rometsch, S. Cao, K. Zhang, X. Wu, Towards a high strength aluminium alloy development methodology for selective laser melting, Mater. Des. 174 (2019) 107775.

[8] A.B. Spierings, K. Dawson, M. Voegtlin, F. Palm, P.J. Uggowitzer, Microstructure and mechanical properties of as-processed scandium-modified

aluminium using selective laser melting, CIRP Ann. - Manuf. Technol. 65 (2016) 213–216.

[9] H. Zhang, D. Gu, J. Yang, D. Dai, T. Zhao, C. Hong, A. Gasser, R. Poprawe, Selective laser melting of rare earth element Sc modified aluminum alloy: Thermodynamics of precipitation behavior and its influence on mechanical properties, Addit. Manuf. 23 (2018) 1–12.

[10] J. Glerum, T. Sun, C. Kenel, D.C. Dunand, Synthesis of Precipitation-Strengthened Al-Sc, Al-Zr and Al-Zr-Sc Alloys via Selective Laser Melting of Elemental Powder Blends, Submitt. to Addit. Manuf. (2020) 101461.

[11] R. Li, M. Wang, Z. Li, P. Cao, T. Yuan, H. Zhu, Developing a high-strength Al-Mg-Si-Sc-Zr alloy for selective laser melting: Crack-inhibiting and multiple strengthening mechanisms, Acta Mater. 193 (2020) 83–98.

[12] A.B. Spierings, K. Dawson, K. Kern, F. Palm, K. Wegener, SLM-processed Sc- and Zr- modified Al-Mg alloy: Mechanical properties and microstructural effects of heat treatment, Mater. Sci. Eng. A. 701 (2017) 264–273.

[13] D. Bayoumy, D. Schliephake, S. Dietrich, X.H. Wu, Y.M. Zhu, A.J. Huang, Intensive processing optimization for achieving strong and ductile Al-Mn-Mg-Sc-Zr alloy produced by selective laser melting, Mater. Des. 198 (2021) 109317.

[14] Q. Jia, P. Rometsch, P. Kürnsteiner, Q. Chao, A. Huang, M. Weyland, L. Bourgeois, X. Wu, Selective laser melting of a high strength Al-Mn-Sc alloy: Alloy design and strengthening mechanisms, Acta Mater. 171 (2019) 108–118.

[15] J. Røyset, N. Ryum, Scandium in aluminium alloys, Int. Mater. Rev. 50 (2005) 19–44.

[16] A.B. Spierings, K. Dawson, T. Heeling, P.J. Uggowitzer, R. Schäublin, F. Palm,

K. Wegener, Microstructural features of Sc- and Zr-modified Al-Mg alloys processed by selective laser melting, Mater. Des. 115 (2017) 52–63.

[17] H. Zhang, D. Gu, D. Dai, C. Ma, Y. Li, R. Peng, S. Li, G. Liu, B. Yang, Influence of scanning strategy and parameter on microstructural feature, residual stress and performance of Sc and Zr modified Al–Mg alloy produced by selective laser melting, Mater. Sci. Eng. A. 788 (2020) 139593.

[18] R. Ma, C. Peng, Z. Cai, R. Wang, Z. Zhou, X. Li, X. Cao, Effect of bimodal microstructure on the tensile properties of selective laser melt Al-Mg-Sc-Zr alloy, J. Alloys Compd. 815 (2020) 152422.

[19] Z. Wang, X. Lin, N. Kang, Y. Hu, J. Chen, W. Huang, Strength-ductility synergy of selective laser melted Al-Mg-Sc-Zr alloy with a heterogeneous grain structure, Addit. Manuf. 34 (2020) 101260.

[20] A.B. Spierings, K. Dawson, P.J. Uggowitzer, K. Wegener, Influence of SLM scan-speed on microstructure, precipitation of Al3Sc particles and mechanical properties in Sc- and Zr-modified Al-Mg alloys, Mater. Des. 140 (2018) 134–143.

[21] R. Ma, C. Peng, Z. Cai, R. Wang, Z. Zhou, X. Li, X. Cao, Enhanced strength of the selective laser melted Al-Mg-Sc-Zr alloy by cold rolling, Mater. Sci. Eng. A. 775 (2020).

[22] R. Ma, C. Peng, Z. Cai, R. Wang, Z. Zhou, X. Li, X. Cao, Manipulating the microstructure and tensile properties of selective laser melted Al–Mg-Sc-Zr alloy through heat treatment, J. Alloys Compd. 831 (2020).

[23] Y. Shi, K. Yang, S.K. Kairy, F. Palm, X. Wu, P.A. Rometsch, Effect of platform temperature on the porosity, microstructure and mechanical properties of an Al–

Mg–Sc–Zr alloy fabricated by selective laser melting, Mater. Sci. Eng. A. 732 (2018) 41–52.

[24] T. DebRoy, S.A. David, J.N. DuPont, T. Koseki, H.K. Bhadeshia, Trends in Welding Research 2012: Proceedings of the 9th International Conference, ASM International, 2013.

[25] Q. Jia, F. Zhang, P. Rometsch, J. Li, J. Mata, M. Weyland, L. Bourgeois, M. Sui, X. Wu, Precipitation kinetics, microstructure evolution and mechanical behavior of a developed Al–Mn–Sc alloy fabricated by selective laser melting, Acta Mater. 193 (2020) 239–251.

[26] K.L. Kendig, D.B. Miracle, Strengthening mechanisms of an Al-Mg-Sc-Zr alloy, Acta Mater. 50 (2002) 4165–4175.

[27] N. Kumar, R.S. Mishra, Additivity of strengthening mechanisms in ultrafine grained Al-Mg-Sc alloy, Mater. Sci. Eng. A. 580 (2013) 175–183.

[28] N. Kumar, R.S. Mishra, C.S. Huskamp, K.K. Sankaran, Critical grain size for change in deformation behavior in ultrafine grained Al-Mg-Sc alloy, Scr. Mater. 64 (2011) 576–579.

[29] R.E. Smallman, A.H.W. Ngan, Modern physical metallurgy, eighth ed., Elsevier, Butterworths, 2014.

[30] T. Ito, Y. Mine, M. Otsu, K. Takashima, Strain measurement of micrometre-sized structures under tensile loading by using scanning white-light interferometry, Mater. Trans. 57 (2016) 1252–1256.

[31] N. Phansalkar, S. More, A. Sabale, M. Joshi, Adaptive local thresholding for detection of nuclei in diversity stained cytology images, in: ICCSP 2011 - 2011 International Conference on Communications and Signal Processing, 2011, pp.

218–220.

[32] D. Legland, I. Arganda-Carreras, P. Andrey, MorphoLibJ: Integrated library and plugins for mathematical morphology with ImageJ, Bioinformatics. 32 (2016) 3532–3534.

[33] J. Schindelin, I. Arganda-Carreras, E. Frise, V. Kaynig, M. Longair, T. Pietzsch, S. Preibisch, C. Rueden, S. Saalfeld, B. Schmid, J.Y. Tinevez, D.J. White, V. Hartenstein, K. Eliceiri, P. Tomancak, A. Cardona, Fiji: An open-source platform for biological-image analysis, Nat. Methods. 9 (2012) 676–682.

[34] D.J. Larson, T.J. Prosa, R.M. Ulfig, B.P. Geiser, T.F. Kelly, Local Electrode Atom Probe Tomography, Springer New York, 2013.

[35] O.C. Hellman, J.A. Vandenbroucke, J. Rüsing, D. Isheim, D.N. Seidman, Analysis of three-dimensional atom-probe data by the proximity histogram, Microsc. Microanal. 6 (2000) 437–444.

[36] A.B. Spierings, K. Dawson, P. Dumitraschkewitz, S. Pogatscher, K. Wegener, Microstructure characterization of SLM-processed Al-Mg-Sc-Zr alloy in the heat treated and HIPed condition, Addit. Manuf. 20 (2018) 173–181.

[37] C.B. Fuller, D.N. Seidman, D.C. Dunand, Mechanical properties of Al(Sc,Zr) alloys at ambient and elevated temperatures, Acta Mater. 51 (2003) 4803–4814.

[38] G. Gottstein, Physical Foundations of Materials Science, Springer Science & Business Media, 2004.

[39] J. Wyrzykowski, M.W. Grabski, Short Communication Liiders deformation in ultrafine-grained pure aluminium, 1982.

[40] N. Tsuji, Y. Ito, Y. Saito, Y. Minamino, Strength and ductility of ultrafine grained aluminum and iron produced by ARB and annealing, Scr. Mater. 47

(2002) 893–899.

[41] C.Y. Yu, P.W. Kao, C.P. Chang, Transition of tensile deformation behaviors in ultrafine-grained aluminum, Acta Mater. 53 (2005) 4019–4028.

[42] P.L. Sun, C.Y. Yu, P.W. Kao, C.P. Chang, Influence of boundary characters on the tensile behavior of sub-micron-grained aluminum, Scr. Mater. 52 (2005) 265–269.

[43] R. Mahmudi, Yield point phenomenon in ultrafine-grained aluminium sheets, Mater. Lett. 19 (1994) 243–246.

[44] D.J. Lloyd, Deformation of fine-grained aluminium alloys, Met. Sci. 14 (1980) 193–198.

[45] D.J. Lloyd, H. Jin, Inhomogeneous yielding and work hardening of a fine grained Al-Mg alloy, Mater. Sci. Eng. A. 585 (2013) 455–459.

[46] R. Schwab, V. Ruff, On the nature of the yield point phenomenon, Acta Mater. 61 (2013) 1798–1808.

[47] A.H. Cottrell, B.A. Bilby, Dislocation Theory of Yielding and Strain Ageing of Iron, Proc. Phys. Soc. A 62 (1949) 49.

[48] B.J. Brindley, P.J. Worthington, Yield-point phenomena in substitutional alloys, Metall. Rev. 15 (1970) 101–141.

[49] D.J. Lloyd, Deformation of fine-grained aluminium alloys, Met. Sci. 14 (1980) 193–198.

[50] M.A. Meyers, A. Mishra, D.J. Benson, Mechanical properties of nanocrystalline materials, Prog. Mater. Sci. 51 (2006) 427–556.

[51] E. V. Kozlov, A.N. Zhdanov, N.A. Koneva, Deformation mechanisms and mechanical properties of nanocrystalline materials, Phys. Mesomech. 11 (2008)

42–50.

[52] D.A. Porter, K.E. Easterling, Phase Transformations in Metals and Alloys, second ed., Chapman & Hall, London, 1992.

[53] C.Q. Chen, J.F. Knott, Effects of dispersoid particles on toughness of high-strength aluminium alloys, Met. Sci. 15 (1981) 357–364.

[54] B. Ahn, S.R. Nutt, Strain mapping of Al-Mg alloy with multi-scale grain structure using digital image correlation method, Exp. Mech. 50 (2010) 117–123.

[55] L. Ladani, S. Nelson, Transition of crack propagation path under varied levels of load in bimodal grain size Al-Mg alloy, J. Eng. Mater. Technol. Trans. ASME. 133 (2011).

[56] B.Q. Han, Z. Lee, D. Witkin, S. Nutt, E.J. Lavernia, Deformation behavior of bimodal nanostructured 5083 Al alloys, Metall. Mater. Trans. A Phys. Metall. Mater. Sci. 36 (2005) 957–965.

[57] R.Q. Ye, B.Q. Han, E.J. Lavernia, Simulation of deformation and failure process in bimodal Al alloys, in: Metallurgical and Materials Transactions A: Physical Metallurgy and Materials Science, 2005, pp. 1833–1840.

[58] Z. Lee, V. Radmilovic, B. Ahn, E.J. Lavernia, S.R. Nutt, Tensile deformation and fracture mechanism of bulk bimodal ultrafine-grained Al-Mg alloy, in: Metallurgical and Materials Transactions A: Physical Metallurgy and Materials Science, 2010, pp. 795–801.

[59] S. Siddique, M. Imran, E. Wycisk, C. Emmelmann, F. Walther, Influence of process-induced microstructure and imperfections on mechanical properties of AlSi12 processed by selective laser melting, J. Mater. Process. Technol. 221 (2015) 205–213.

[60] K. V. Yang, Y. Shi, F. Palm, X. Wu, P. Rometsch, Columnar to equiaxed transition in Al-Mg(-Sc)-Zr alloys produced by selective laser melting, Scr. Mater. 145 (2018) 113–117.

[61] X. Liu, C. Zhao, X. Zhou, Z. Shen, W. Liu, Microstructure of selective laser melted AlSi10Mg alloy, Mater. Des. 168 (2019) 107677.

[62] E.O. Hall, The deformation and ageing of mild steel: III Discussion of Results, Proc. Phys. Soc. Sect. B. 64 (1951) 747.

[63] Ø. Ryen, O. Nijs, E. Sjölander, B. Holmedal, H.E. Ekström, E. Nes, Strengthening mechanisms in solid solution aluminum alloys, Metall. Mater. Trans. A Phys. Metall. Mater. Sci. 37 (2006) 1999–2006.

[64] K. Dinsdale, S.J. Harris, B. Noble, Relationship between microstructure and mechanical properties of aluminium-lithium-magnesium alloys, in: T.H. Sanders, E.A. Starke (Eds.), TMS Proceedings, 1981, pp. 102–118.

[65] Y. Guo, B. Liu, W. Xie, Q. Luo, Q. Li, Anti-phase boundary energy of β series precipitates in Mg-Y-Nd system, Scr. Mater. 193 (2021) 127–131.

[66] A.J. Ardell, Precipitation Hardening, Metall. Trans. A. 16 (1985) 2131–2165.

[67] D. Seidman, E. Marquis, D. Dunand, Precipitation strengthening at ambient and elevated temperatures of heat-treatable Al (Sc) alloys, Acta Mater. 50 (2002) 4021–4035.

[68] K.E. Knipling, R.A. Karnesky, C.P. Lee, D.C. Dunand, D.N. Seidman, Precipitation evolution in Al-0.1Sc, Al-0.1Zr and Al-0.1Sc-0.1Zr (at.%) alloys during isochronal aging, Acta Mater. 58 (2010) 5184–5195.

[69] K. Ma, H. Wen, T. Hu, T.D. Topping, D. Isheim, D.N. Seidman, E.J. Lavernia, J.M. Schoenung, Mechanical behavior and strengthening mechanisms in ultrafine

grain precipitation-strengthened aluminum alloy, Acta Mater. 62 (2014) 141–155.

[70] L.A. Gypen, A. Deruyttere, Multi-component solid solution hardening - Part 1 Proposed model, J. Mater. Sci. 12 (1977) 1028–1033.